npj | 2D Materials and Applications

www.nature.com/npj2dmaterials

ARTICLE OPEN

Check for updates

In-plane anisotropic optical and mechanical properties of two-dimensional MoO_3

Sergio Puebla[1], Roberto D'Agosta[2,3], Gabriel Sanchez-Santolino[4], Riccardo Frisenda[1], Carmen Munuera[1] and Andres Castellanos-Gomez[1]✉

Molybdenum trioxide (MoO_3) in-plane anisotropy has increasingly attracted the attention of the scientific community in the last few years. Many of the observed in-plane anisotropic properties stem from the anisotropic refractive index and elastic constants of the material but a comprehensive analysis of these fundamental properties is still lacking. Here we employ Raman and micro-reflectance measurements, using polarized light, to determine the angular dependence of the refractive index of thin MoO_3 flakes and we study the directional dependence of the MoO_3 Young's modulus using the buckling metrology method. We found that MoO_3 displays one of the largest in-plane anisotropic mechanical properties reported for 2D materials so far.

npj 2D Materials and Applications (2021)5:37 ; https://doi.org/10.1038/s41699-021-00220-5

INTRODUCTION

Recently, two-dimensional (2D) materials with an in-plane anisotropy, such as several transition metal chalcogenides, group-VA, black phosphorus and compounds made of two group-VA elements (so called V-V binary materials), have been extensively studied[1–21]. Some of them have demonstrated a great potential in optoelectronics and flexible electronics applications[22–25], allowing the fabrication of devices with new functionalities (e.g., polarization sensitive photodetectors[22,26]) and the observation of quasi one-dimensional physics phenomena[27]. Among the available anisotropic 2D materials, molybdenum trioxide is a wide band gap semiconductor (>2.7 eV)[28], which makes it quasi-transparent in the visible spectrum while being still electrically conductive. This nanomaterial has been proven useful for gas sensing[29], resistive memory technology[30], optoelectronic[31–40], electrochromic[41] and flexible[42,43] applications. The difference between the in-plane (*a*-*c*) lattice parameters makes α-MoO_3 a perfect candidate to investigate optical, mechanical, and electrical in-plane anisotropic properties. Indeed, calculations show that in-plane carrier mobility exhibit strong anisotropic behavior[44] and highly anisotropic propagation of phonon polaritons have been recently observed in α-MoO_3[45–48]. In comparison with metallic plasmon polaritons, phonon polaritons can achieve reduced optical losses, improved light confinements and higher quality factors[49–52]. These interesting optical properties are mainly caused by the anisotropy of the fundamental properties of molybdenum trioxide, which until now have been scarcely investigated.

Here, using a combination of experiments and density functional theory calculations, we have studied the direction-dependent refractive index (birefringence) and Young's Modulus of α-MoO_3 exfoliated flakes, two fundamental quantities that govern the anisotropy observed in Raman and phonon polariton experiments. We studied thin flakes of α-MoO_3 by aberration-corrected scanning transmission electron microscopy and energy-dispersive x-ray spectroscopy. We then deposited the flakes on SiO_2/Si substrates and identified the crystallographic orientation of samples using angle-resolved polarized Raman spectroscopy technique[53]. Then, we determined the in-plane anisotropy of the MoO_3 refractive index using angle-resolved polarized micro-reflectance spectroscopy, finding a remarkably large birefringence. The anisotropic mechanical properties of the MoO_3 flakes was experimentally investigated with the buckling metrology method[54,55], finding one of the largest Young's modulus anisotropy reported so far for 2D materials.

RESULTS

Crystal structure study

We have grown MoO_3 flakes in atmospheric conditions using a modified version of the hot plate-based physical vapor transport method described in ref. [56]. Briefly, a molybdenum foil was oxidized on a hotplate at 540 °C, then a silicon wafer was placed on top. At this temperature, the molybdenum oxide sublimes and re-crystallizes on the surface of the Si wafer, which is at a slightly lower temperature, forming MoO_3 flakes. Then, a Gel-Film (Gel-Pak WF x4 6.0 mil) stamp is used to pick-up and exfoliate the MoO_3 flakes. These flakes can be then transferred onto a target substrate (e.g., a holey Si_3N_4 TEM grid or a 297 nm SiO_2/Si substrate) using deterministic transfer set up (see Materials and Methods section for more information).

Figure 1a shows the layered crystal structure of α-MoO_3[57–59], belonging to the *Pbnm* space group. It consists of a double-layer stacking of linked distorted MoO_6 octahedra in the *b* direction, along which the adjacent layers are linked by weak van der Waals forces, while in-plane atoms are strongly bonded. This configuration leads to lattice parameters: a = 3.96 Å, b = 13.86 Å and c = 3.70 Å (JCPDS file: 05-0508)[44,53,56,59,60]. We characterized the structure and composition of the grown MoO_3 flakes using scanning transmission electron microscopy (STEM) along with energy dispersive x-ray spectroscopy (EDS) and scanning electron microscopy (see Supplementary Fig. 4 in the Supporting

[1]Materials Science Factory. Instituto de Ciencia de Materiales de Madrid (ICMM-CSIC), Madrid, Spain. [2]Nano-Bio Spectroscopy Group and European Theoretical Spectroscopy Facility (ETSF), Departamento Polímeros y Materiales Avanzados: Física, Química y Tecnología, Universidad del País Vasco UPV/EHU, San Sebastián, Spain. [3]IKERBASQUE, Basque Foundation for Science, Bilbao, Spain. [4]GFMC, Departamento de Física de Materiales & Instituto Pluridisciplinar, Universidad Complutense de Madrid, Madrid, Spain. ✉email: andres.castellanos@csic.es

Published in partnership with FCT NOVA with the support of E-MRS

npj nature partner journals

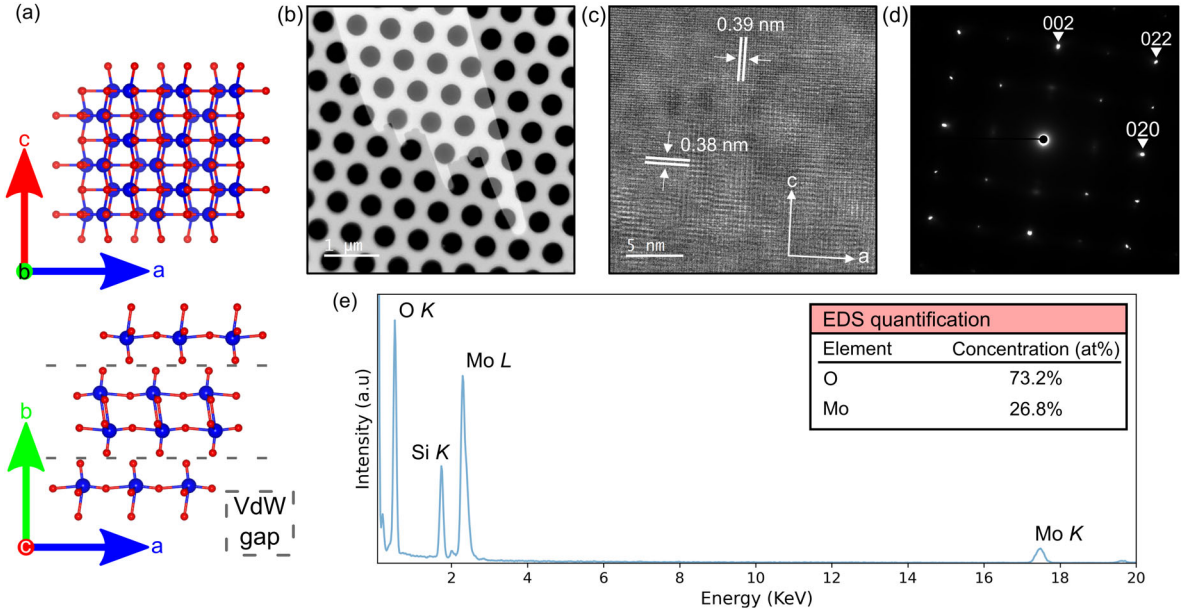

Fig. 1 Anisotropic structure of MoO_3 flakes. a Crystal structure of MoO_3 in Pbnm notation, spheres in blue (red) represent Mo (O) atoms, the two different views belong to ca (top), and ba plane projection (bottom). **b** Low magnification HAADF image of a mechanically exfoliated MoO_3 flake transferred over a porous SiN membrane, scale bar is of 1 μm. **c** Atomic resolution HAADF image depicting the anisotropy between the in-plane (**a**–**c**) lattice parameters, scale bar is of 5 nm. **d** SAED pattern characteristic of the orthorhombic α- MoO_3. **e** EDS spectrum taken at the flake shown in **b**.

Information). A thin flake was transferred into a porous Si_3N_4 membrane, as shown in Fig. 1b. Atomic resolution high angle annular dark field (HAADF) imaging shows an orthorhombic α-MoO_3 structure with a difference in the *a*-*c* lattice parameters, as depicted also in a selected area diffraction pattern (SAED) acquired at the same flake (Fig. 1c, d)[44,53,56,59,60]. The chemical composition of the flake was determined by EDS, Fig. 1e shows the spectrum of MoO_3 used for quantification, where we find a small oxygen deficiency.

Angle-resolved polarized Raman spectroscopy analysis

We have used angle-resolved polarized Raman spectroscopy technique to identify the different crystal directions in our MoO_3 flakes. Using a linearly polarized laser in a Raman system (see Materials and Methods section) and setting the analyzer and polarizer in a parallel configuration, while we rotate the sample, we obtain the spectra shown in Fig. 2a. The system set up is depicted in Supplementary Fig. 1 in the Supplementary Information and it is explained in detail by Liu et al.[61]. Typical MoO_3 Raman modes are A_g and B_g[62] and no correlation has been found between the Raman modes and the MoO_3 thickness[63]. We highlight the peaks centered at 282 cm^{-1}, assigned to B_{2g} mode, and at 156 and 818 cm^{-1}, assigned to A_g^c and A_g^a mode, respectively. The A_g^c peak corresponds to the translation vibration of the rigid MoO_6 octahedra chains along the c-axis, and the A_g^a mode is the asymmetric stretching vibration of O-Mo-O atoms along the a-axis[53,62].

We have carried out angle-resolved polarized Raman measurements in a MoO_3 flake of 28 nm of thickness from 0° to 360°, with a step of 4°. The thickness has been determined by combination of atomic force microscopy with recently developed optical microscopy based techniques[64]. In Fig. 2a three of these measurements at different angles (0°, 45° and 90°) are displayed. Notice the difference in intensity of each mode, revealing how the relative orientation between the incident laser polarization angle and the direction of the crystalline axes plays an important role in the Raman process. In fact, previous works have shown how the A_g and B_{2g} mode intensities can be fitted to[53,62]:

$$I(A_g) \propto \left(A\cos^2\beta + C\sin^2\beta\right)^2 \quad (1)$$

$$I(B_{2g}) \propto E^2 \sin^2 2\beta \quad (2)$$

where β is the relative angle between the a-axis crystal direction and the linear polarization direction of the laser. Figure 2b shows the normalized intensity angle-resolved polarized Raman measurements of each mode (light red), with the resulting fit to Eqs. (1) and (2) (in dark red), showing an excellent agreement. Note, the A_g^c and A_g^a modes are useful to extract the crystal structure of the sample due to their 180-degree periodicity. The inset in Fig. 2a shows a microscopy image of the MoO_3 flake on SiO_2/Si, studied with the Raman spectroscopy. The a- and c-axes, determined from the Raman measurements are depicted in the figure and coincide with the straight edges produced during the exfoliation of the MoO_3 flake.

Polarized micro-reflectance analysis

In order to gain an insight about the in-plane anisotropic optical properties of MoO_3 flakes we carried out micro-reflectance measurements employing linearly polarized incident light. Figure 3 shows the optical contrast spectra acquired for different alignment between the crystal axis and the incident linear polarization (see the bottom inset). The optical contrast *C* is defined as:

$$C = \frac{I_{fl} - I_{sub}}{I_{fl} + I_{sub}} \quad (3)$$

where I_{fl} and I_{sub} are the intensity measured on the MoO_3 flake and on the bare substrate, respectively. Interestingly, it has been demonstrated how one can use a simple Fresnel law-based model to accurately reproduce the measured optical contrast spectra[64]. Moreover, given the known refractive indexes of air, SiO_2 and Si and the known thickness of the SiO_2 film and MoO_3 flake one can determine the refractive index of the MoO_3 flake for different alignment between the incident linearly polarized light and the crystal directions by using the refractive index as a fitting

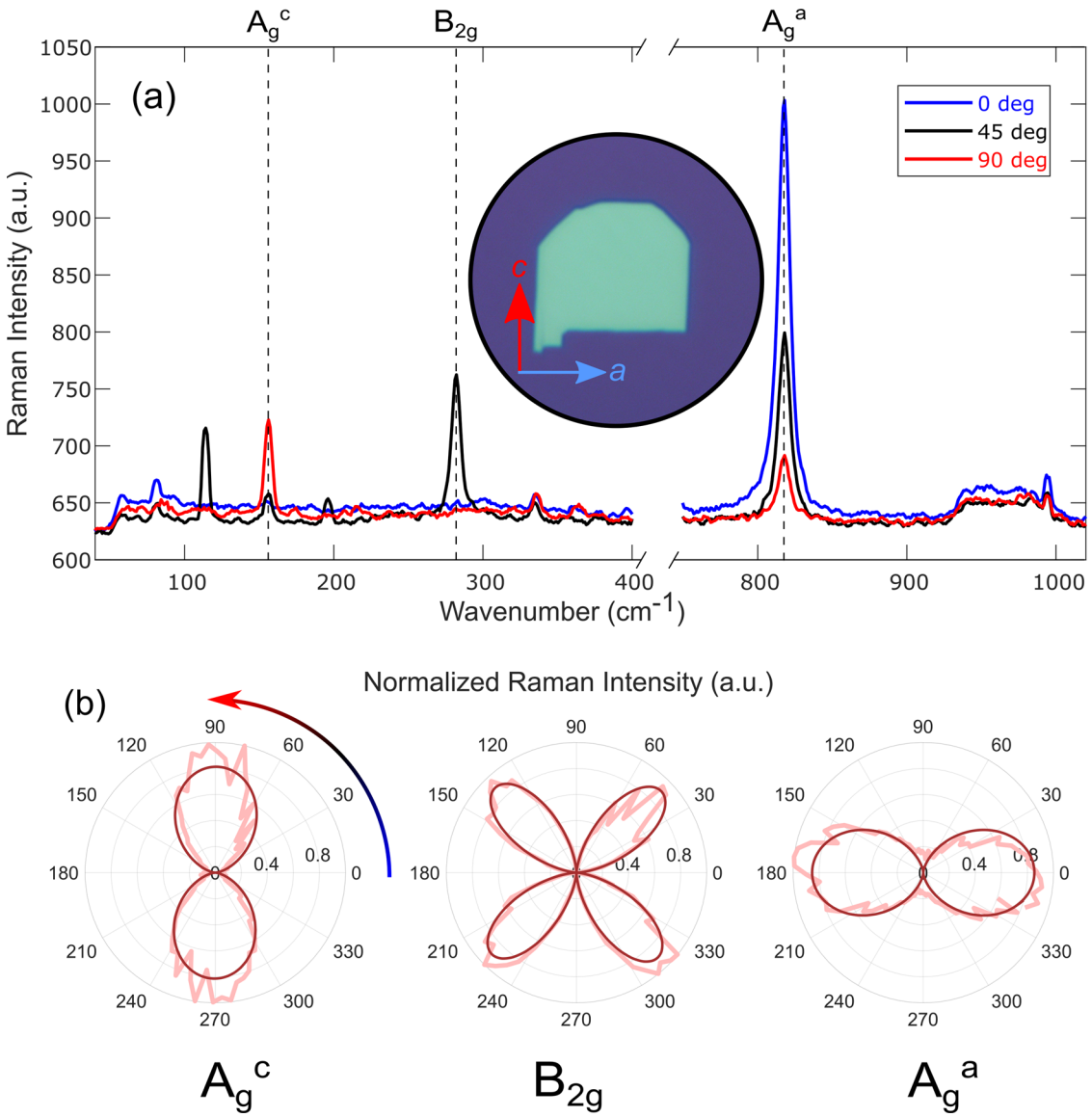

Fig. 2 Determining the crystal orientation of MoO_3 through Raman spectroscopy. a Raman spectra at 0° (blue), 45° (black) and 90° (red) angles with respect to the horizontal axis. A_g^c, B_{2g} and A_g^a Raman modes are highlighted with vertical dashed lines. Inset: Microscopy image of the sample placed in the initial position (0°) and the a and c axes, determined from the angle-resolved Raman measurements, are shown. **b** Polar plots, in light red; and fittings, in dark red, of angle-resolved normalized Raman intensities of the A_g^c (left), B_{2g} (middle) and A_g^a (right) modes.

parameter to achieve the best fit of the Fresnel law-based model to the experimental data. The top inset in Fig. 3 shows the resulting in-plane angular dependence of the refractive index displaying a marked anisotropy (birefringence). While along the a-axis the refractive index of MoO_3 is $n_a = 2.21 + 0i$, along the c-axis the refractive index increases up to $n_c = 2.30 + 0i$. The difference Δn between n_c and n_a, is ~0.1. This value is comparable to that of well-known strongly birefringent materials like calcite (−0.17) and barium borate (−0.12)[65,66]. If we compare it with other anisotropic 2D materials, the birefringence of MoO_3 is larger than that of ReS_2 and $ReSe_2$ (~0.04)[6] but substantially lower than the values reported for black phosphorus (0.25)[6] or TiS_3 (0.3)[67]. However, note that, unlike MoO_3, all these anisotropic 2D materials are rather opaque in the visible range of the electromagnetic spectrum, limiting their application in polarization optics applications. Therefore, the birefringence value of MoO_3, although more modest in comparison with TiS_3 or black phosphorus, can have a stronger impact in future ultrathin polarization optics applications.

These experimental results for MoO_3 are confirmed by theoretical ab-initio calculations through the solution of the Bethe–Salpeter's equation, in which we have obtained refractive index values of $n_a = 2.40$ and $n_c = 2.60$ at small frequency, with a difference $\Delta n \sim 0.2$. We find these theoretical values close to the ones obtained experimentally. We attribute the lower birefringence experimental value to the presence of defects in the MoO_3 flakes, not considered in the calculations, that can effectively reduce the anisotropy of the lattice.

Mechanical anisotropy study

In the following we focus on the characterization of the anisotropy of the Young's modulus, one of the fundamental magnitudes that govern the mechanical properties of materials, of MoO_3 flakes. We use buckling induced metrology method, which has been proved to be an easy, but reliable way to study the Young's modulus of thin films[54,55] and 2D materials[68–72]. The method relies on studying the buckling instability that arises when a thin film is

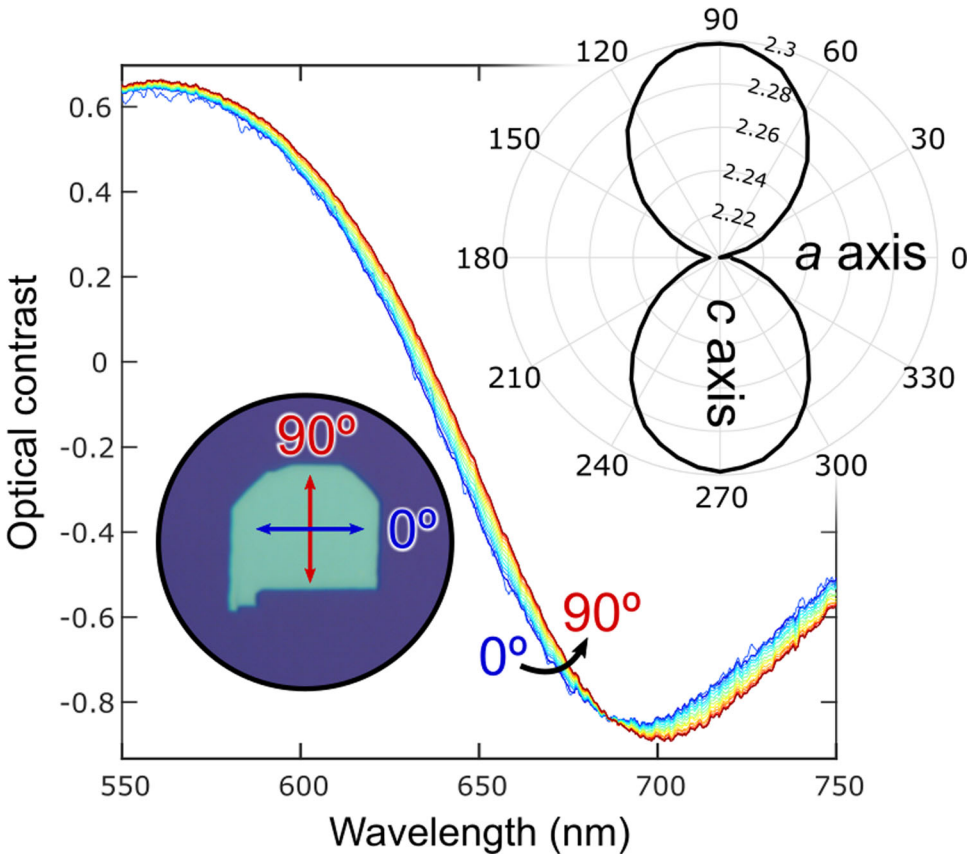

Fig. 3 Birefringence of MoO_3 flakes. Optical contrast *vs*. wavelength spectra, measured for the 28 nm thick MoO_3 flake shown in the bottom inset, as function of the angle formed between the incident linearly polarized light and the crystal a-axis. Top inset: Polar plot of the change in refractive index as a function of the relative orientation between the incident linearly polarized light and the a-axis of the crystal.

deposited onto an adhesive compliant substrate, and it is subjected to in-plane uniaxial compression[73]. Because of this compression, there is a trade-off in the energy related to the adhesion forces between film and substrate and the bending rigidity of the film. This trade-off leads to a rippling pattern of the thin film, which is characteristic of the film and substrate properties (in the Supplementary Information it can be found an animated GIF, Supplementary GIF, of a α-MoO_3 flake compressed in this way). To perform the buckling metrology measurements, the MoO_3 flakes were transferred onto a flat (unstrained) Gel-Film substrate that is mounted on a rotation stage under the inspection of an optical microscope. Then the flakes were subjected to compressive strain along different crystal directions by pinching the surface of the Gel-Film with two glass slides and pictures of the obtained ripple patterns are acquired with a digital camera attached to the microscope. The MoO_3 flakes are then transferred to a SiO_2/Si substrate to determine their crystal orientation, through Raman spectroscopy and micro-reflectance, and thickness through AFM (see Supplementary Figs. 2 and 3 of the Supporting Information).

The wavelength, λ, of the rippling pattern can be used to determine the Young's modulus:

$$E_f = 3\left(\frac{\lambda}{2\pi h}\right)^3 \frac{1 - \nu_{fa}\nu_{fc}}{1 - \nu_s^2} E_s \quad (4)$$

being h the flake thickness, ν_s, ν_f, E_s and E_f the Poisson's ratio and Young's Modulus of substrate and flake, respectively. The Poisson's ratio of α-MoO_3 must be taken along the two axes. Using density functional theory (more details available in the Supplementary Information) we calculate Poisson's ratios of α-MoO_3 correspond to $\nu_{fa} = 0.147$ and $\nu_{fc} = 0.06$. In our experiment we used a Gel-Film substrate as compliant substrate, with $\nu_{sub} = 0.5$[74] and its Young's Modulus is $E_{sub} = 492 \pm 11$ kPa[68].

Figure 4a shows optical images of a 24 nm thick MoO_3 flake (thickness and orientation obtained with optical microscopy based technique, shown in Supplementary Fig. 2) when it is subjected to compression along the a- and c-axes. Upon compression along different orientations the MoO_3 develops a rippled pattern whose periodicity depends on the direction. In Fig. 4b, a statistical study is shown with 14 different samples with thicknesses ranging from 18 to 62 nm (white circles), from which we obtain the mean Young's Modulus values and their standard deviation along the a- and c-axis. We use histograms to show the flake-to-flake variability of these results and we fit them with a normalized Gaussian distribution function. Moreover, we plot the corresponding two-dimensional normalized Gaussian distribution function in a 2D gray colormap, in which the density of datapoints is associated with the colorbar, set as inset. The obtained Young's modulus values along the a- and c-axes directions are $E_{\text{a-axis}} = 44 \pm 8$ GPa and $E_{\text{c-axis}} = 86 \pm 15$ GPa, respectively. Interestingly the anisotropy ratio ($E_{\text{c-axis}}/E_{\text{a-axis}}$) is ~2 among the largest value reported in the literature for anisotropic 2D materials: black phosphorus ~2.7[17], for orpiment (As_2S_3) is ~1.7[75]. Our DFT calculations predict even higher Young's modulus values (91.9 GPa and 216.9 GPa for the a- and c-axis respectively) in relatively good agreement with the values reported for bulk-like MoO_3 (~200 nm thick) crystals through Brillouin scattering. Note that the presence of defects in the synthesized MoO_3 samples, like the oxygen vacancies found in the STEM-EDS analysis, could explain the lower Young's modulus values obtained in our experiments.

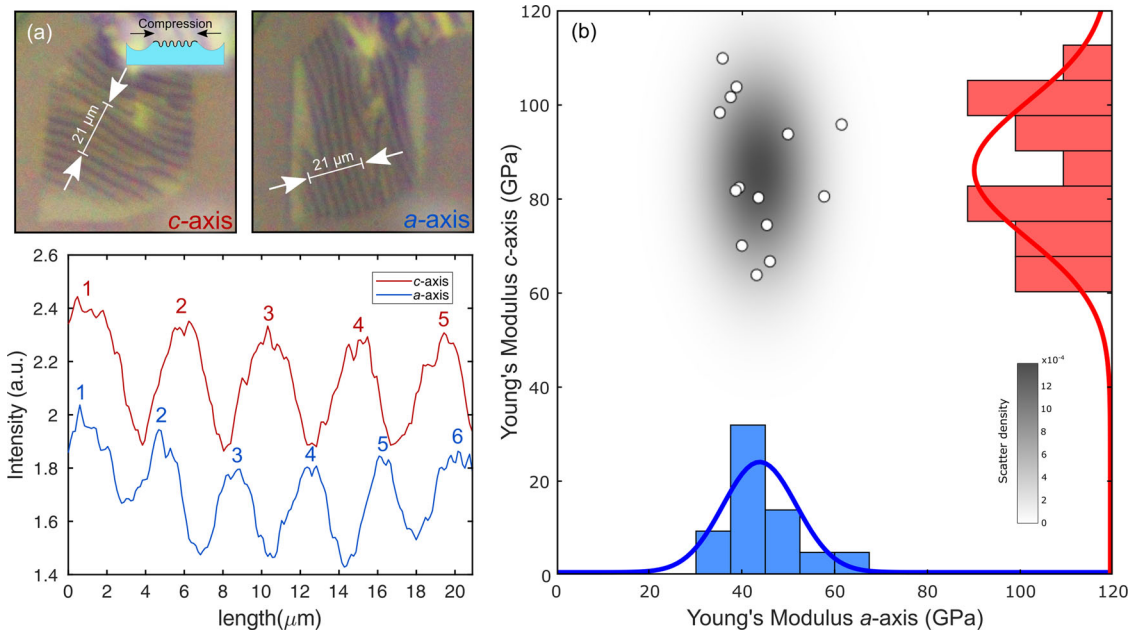

Fig. 4 Anisotropic mechanical properties of MoO_3 flakes. a Optical images of a MoO_3 flake on Gel-Film substrate applying compression along a and c axes (top images), inset: process of ripples formation; determination of the wavelength of periodic ripples (bottom figure). **b** Scatter density plot of Young's modulus values along the two directions obtained from 14 different samples, white circles with black edges, and fitted with a multivariate Gaussian normal distribution function, in gray. Inset: Histogram plots of Young's modulus along the a-axis (blue) and the c-axis (red), fitted with a Gaussian distribution.

DISCUSSION

In summary, we combined scanning transmission electron microscopy, Raman spectroscopy, micro-reflectance and buckling metrology to probe the anisotropic optical and mechanical properties of exfoliated MoO_3 flakes. We found that the flakes show a strong birefringence, i.e., their refractive index depends on the alignment between the polarization of the incident light and the crystalline axis. The difference between the refractive index for light polarized along the a- and c-axes reaches ~0.1. This large value, together with the fact that MoO_3 is transparent in the visible range, makes this material a good candidate for future polarization optics applications. Regarding the mechanical properties, we found that the experimental Young's modulus along the a- and c-axes directions are $E_{\text{a-axis}} = 44 \pm 8$ GPa and $E_{\text{c-axis}} = 86 \pm 15$ GPa, respectively, yielding an anisotropy ratio of ~2, only surpassed by black phosphorus. Our results agree with ab-initio calculations of optical and elastic properties of MoO_3. The anisotropy in the refractive index and the Young's modulus have strong impact in many optical and mechanical properties and thus, we believe that our work can be used as the foundation of further works studying the intriguing anisotropic properties of MoO_3.

METHODS

Growth and deposition

We have based our present grown procedure on a modification of the hot plate growth method developed by Molina-Mendoza et al.[56].

Once the growth of the crystals is finished, the MoO_3 flakes are firstly exfoliated onto a polydimethylsiloxane (PDMS) (Gel-Film WF x4 6.0 mil, by Gelpak®) and then transferred onto a 297 nm SiO_2/Si substrate using a deterministic transfer method[76,77].

Scanning transmission electron microscopy

For the scanning transmission electron microscope characterization, we used an aberration-corrected JEOL JEM-ARM 200cF electron microscope operated at 80 kV, equipped with a cold field emission gun and an Oxford Instruments EDS spectrometer.

Optical microscopy and spectroscopy

Optical microscopy images were acquired using a Motic BA310 MET-T microscope equipped with a 50 × 0.55 NA objective and an AMScope MU1803 CMOS Camera. Reflection spectra were collected from a spot of ~1.5–2 μm diameter with a Thorlabs CCS200/M fiber-coupled spectrometer (Thorlabs Inc., Newton, New Jersey, United States). More details about the micro-reflectance setup can be found in Reference[78].

Raman spectroscopy

Raman characterization of MoO_3 flakes on 297 nm SiO_2/Si substrates were carried out with a confocal Raman microscopy system (MonoVista CRS+ from Spectroscopy & Imaging GmbH) using a 532 nm excitation laser with an incident power of 1.234 mW and a 100× objective with the integration time of 20 s.

Numerical methods

We have analyzed the optical and elastic properties of MoO_3 using the YAMBO and Quantum Espresso suite of programs[79–81]. For the electronic structure calculation we have used the generalized gradient approximation in the PBE parametrization for the exchange-correlation energy with a plane wave cut-off of 60 Ry[82]. The electronic structure calculations are performed on a Monkhorst-Pack grid of 8 × 8 × 8 points. We have chosen norm-conserving pseudo potentials in the SG15 database[83].

For the elastic properties, we have used the thermo_pw code from the Quantum Espresso suite[84]. The elastic properties agree when we used either norm-converting or ultra-soft pseudo potentials.

DATA AVAILABILITY

Data presented in this study are available on request from the authors.

Received: 20 January 2021; Accepted: 16 March 2021;
Published online: 12 April 2021

REFERENCES

1. Wei, Q. & Peng, X. Superior mechanical flexibility of phosphorene and few-layer black phosphorus. *Appl. Phys. Lett.* **104**, 251915 (2014).

2. Zheng, Q. et al. In-plane anisotropic raman response and electrical conductivity with robust electron-photon and electron-phonon interactions of air stable MoO_2 nanosheets. *J. Phys. Chem. Lett.* **10**, 2182–2190 (2019).
3. Huang, S. et al. In-plane optical anisotropy of layered gallium telluride. *ACS Nano* **10**, 8964–8972 (2016).
4. Zhou, X. et al. Ultrathin 2D GeSe2 rhombic flakes with high anisotropy realized by Van der Waals epitaxy. *Adv. Funct. Mater.* **27**, 1–9 (2017).
5. Kong, W. et al. Angle resolved vibrational properties of anisotropic transition metal trichalcogenide nanosheets. *Nanoscale* **9**, 4175–4182 (2017).
6. Yang, H. et al. Optical waveplates based on birefringence of anisotropic two-dimensional layered materials. *ACS Photonics* **4**, 3023–3030 (2017).
7. Chenet, D. A. et al. In-plane anisotropy in mono- and few-layer ReS2 probed by raman spectroscopy and scanning transmission electron microscopy. *Nano Lett.* **15**, 5667–5672 (2015).
8. Wolverson, D., Crampin, S., Kazemi, A. S., Ilie, A. & Bending, S. J. Raman spectra of monolayer, few-layer, and bulk ReSe2: an anisotropic layered semiconductor. *ACS Nano* **8**, 11154–11164 (2014).
9. Hafeez, M., Gan, L., Li, H., Ma, Y. & Zhai, T. Chemical vapor deposition synthesis of ultrathin hexagonal ReSe2 flakes for anisotropic raman property and optoelectronic application. *Adv. Mater.* **28**, 8296–8301 (2016).
10. Xiong, W., Huang, K. & Yuan, S. The mechanical, electronic and optical properties of two-dimensional transition metal chalcogenides MX2 and M2X3 (M = Ni, Pd; X = S, Se, Te) with hexagonal and orthorhombic structures. *J. Mater. Chem. C.* **7**, 13518–13525 (2019).
11. Zhang, S. et al. Recent progress in 2D group-VA semiconductors: from theory to experiment. *Chem. Soc. Rev.* **47**, 982–1021 (2018).
12. Zhao, P. et al. Giant anisotropic photogalvanic effect in a flexible AsSb monolayer with ultrahigh carrier mobility. *Phys. Chem. Chem. Phys.* **19**, 27233–27239 (2017).
13. Li, L. et al. Emerging in-plane anisotropic two-dimensional materials. 54–73, https://doi.org/10.1002/inf2.12005 (2019).
14. Guo, S. et al. 2D V-V binary materials: status and challenges. *Adv. Mater.* **31**, 1–19 (2019).
15. Frisenda, R. et al. Symmetry breakdown in franckeite: spontaneous strain, rippling, and interlayer Moiré. *Nano Lett.* **20**, 1141–1147 (2020).
16. Xia, F., Wang, H. & Jia, Y. Rediscovering black phosphorus as an anisotropic layered material for optoelectronics and electronics. *Nat. Commun.* **5**, 1–6 (2014).
17. Vaquero-Garzon, L., Frisenda, R. & Castellanos-Gomez, A. Anisotropic buckling of few-layer black phosphorus. *Nanoscale* **11**, 12080–12086 (2019).
18. Island, J. O. et al. Titanium trisulfide (TiS3): a 2D semiconductor with quasi-1D optical and electronic properties. *Sci. Rep.* **6**, 1–7 (2016).
19. Beams, R. et al. Characterization of few-layer 1T′ MoTe2 by polarization-resolved second harmonic generation and Raman scattering. *ACS Nano* **10**, 9626–9636 (2016).
20. Qiu, G. et al. Observation of optical and electrical in-plane anisotropy in high-mobility few-layer ZrTe 5. *Nano Lett.* https://doi.org/10.1021/acs.nanolett.6b02629 (2016).
21. Li, L. et al. Strong in-plane anisotropies of optical and electrical response in layered dimetal chalcogenide. *ACS Nano* **11**, 10264–10272 (2017).
22. Yuan, H. et al. Polarization-sensitive broadband photodetector using a black phosphorus vertical p-n junction. *Nat. Nanotechnol.* **10**, 707–713 (2015).
23. Wang, X. et al. Short-wave near-infrared linear dichroism of two-dimensional germanium selenide. *J. Am. Chem. Soc.* **139**, 14976–14982 (2017).
24. Gong, C. et al. Electronic and optoelectronic applications based on 2D novel anisotropic transition metal dichalcogenides. *Adv. Sci.* **4**, 1700231 (2017).
25. Zhao, Q. et al. Flexible and anisotropic properties of monolayer MX 2 (M = Tc and Re; X = S, Se). *J Phys. Chem.* **2**, 23744–23751 (2017).
26. Niu, Y. et al. Polarization-sensitive and broadband photodetection based on a mixed-dimensionality TiS3/Si p–n junction. *Adv. Opt. Mater.* **6**, 1–7 (2018).
27. Xing, B., Yu, Z., Fu, L., Qin, Q. & Lu, Y. Extraordinarily bound quasi-one-dimensional trions in two-dimensional phosphorene atomic semiconductors. *ACS Nano.* https://doi.org/10.1021/acsnano.5b06193 (2016).
28. Bouzidi, A. et al. Effect of substrate temperature on the structural and optical properties of MoO_3 thin films prepared by spray pyrolysis technique. *Mater. Sci. Eng. B Solid-State Mater. Adv. Technol.* **97**, 5–8 (2003).
29. Rahman, F. et al. Dual selective gas sensing characteristics of 2D α-MoO_{3-x} via a facile transfer process. *ACS Appl. Mater. Interfaces* **11**, 40189–40195 (2019).
30. Rahman, F. et al. Reversible resistive switching behaviour in CVD grown, large area MoOX. *Nanoscale* **10**, 19711–19719 (2018).
31. Guo, Y. et al. Eighteen functional monolayer metal oxides: wide bandgap semiconductors with superior oxidation resistance and ultrahigh carrier mobility. *Nanoscale Horiz.* **4**, 592–600 (2019).
32. Balendhran, S. et al. Enhanced charge carrier mobility in two-dimensional high dielectric molybdenum oxide. *Adv. Mater.* **25**, 109–114 (2013).
33. Kanai, K. et al. Electronic structure of anode interface with molybdenum oxide buffer layer. *Org. Electron.* **11**, 188–194 (2010).
34. Shrotriya, V., Li, G., Yao, Y., Chu, C. W. & Yang, Y. Transition metal oxides as the buffer layer for polymer photovoltaic cells. *Appl. Phys. Lett.* **88**, 1–4 (2006).
35. You, H., Dai, Y., Zhang, Z. & Ma, D. Improved performances of organic light-emitting diodes with metal oxide as anode buffer. *J. Appl. Phys.* **101**, 1–4 (2007).
36. Du, J. et al. Pressure-assisted fabrication of organic light emitting diodes with MoO_3 hole-injection layer. *J. Appl. Phys.* **115**, 233703 (2014).
37. Meyer, J., Shu, A., Kröger, M. & Kahn, A. Effect of contamination on the electronic structure and hole-injection properties of MoO_3/organic semiconductor interfaces. *Appl. Phys. Lett.* **96**, 8–11 (2010).
38. de Castro, I. A. et al. Molybdenum oxides – from fundamentals to functionality. *Adv. Mater.* **29**, 1–31 (2017).
39. Balendhran, S. et al. Large-area synthesis of two-dimensional MoO_{3-x} for enhanced optoelectronic applications. *2D Mater.* **6**, 035031 (2019).
40. Balendhran, S. et al. Two-dimensional molybdenum trioxide and dichalcogenides. *Adv. Funct. Mater.* **23**, 3952–3970 (2013).
41. Arash, A. et al. Electrically Activated UV - A Filters Based on Electrochromic MoO_{3-x}. *ACS Appl. Mater. Interfaces* https://doi.org/10.1021/acsami.9b20916 (2020).
42. Cho, E., Cha, S., Kim, Y. & Kim, C. Transparent and flexible electrode composed of a graphene multilayer interlayer-doped with MoO_3. *Org. Electron.* **77**, 105437 (2020).
43. Han, Y. C., Lim, M. S., Park, J. H. & Choi, K. C. ITO-free flexible organic light-emitting diode using ZnS/Ag/MoO_3 anode incorporating a quasi-perfect Ag thin film. *Org. Electron.* **14**, 3437–3443 (2013).
44. Zhang, W. B., Qu, Q. & Lai, K. High-mobility transport anisotropy in few-layer MoO_3 and its origin. *ACS Appl. Mater. Interfaces* **9**, 1702–1709 (2017).
45. Ma, W. et al. In-plane anisotropic and ultra-low-loss polaritons in a natural van der Waals crystal. *Nature* **562**, 557–562 (2018).
46. Zheng, Z. et al. A mid-infrared biaxial hyperbolic van der Waals crystal. *Sci. Adv.* 1–9 eaav8690 (2019).
47. Chen, M. et al. Configurable phonon polaritons in twisted α-MoO_3. *Nat. Mater.* **19**, 1307–1311 (2020).
48. Zheng, Z. et al. Phonon polaritons in twisted double-layers of hyperbolic van der Waals crystals. *Nano Lett.* **20**, 5301–5308 (2020).
49. Zheng, Z. et al. Highly confined and tunable hyperbolic phonon polaritons in Van Der Waals semiconducting transition metal oxides. *Adv. Mater.* **30**, 1705318 (2018).
50. Wang, T., Li, P., Hauer, B., Chigrin, D. N. & Taubner, T. Optical properties of single infrared resonant circular microcavities for surface phonon polaritons. *Nano Lett.* **13**, 5051–5055 (2013).
51. Summary, R., Basov, D. N., Fogler, M. M. & García De Abajo, F. J. Polaritons in van der Waals materials. *Science* **354**, aag1992 (2016).
52. Low, T. et al. Polaritons in layered two-dimensional materials. *Nat. Mater.* **16**, 182–194 (2016).
53. Zheng, B., Wang, Z., Chen, Y., Zhang, W. & Li, X. Centimeter-sized 2D α-MoO_3 single crystal: growth, Raman anisotropy, and optoelectronic properties. *2D Mater.* **5**, 045011 (2018).
54. Stafford, C. M. et al. A buckling-based metrology for measuring the elastic moduli of polymeric thin films. *Nat. Mater.* **3**, 545–550 (2004).
55. Khang, D. Y., Rogers, J. A. & Lee, H. H. Mechanical buckling: mechanics, metrology, and stretchable electronics. *Adv. Funct. Mater.* **19**, 1526–1536 (2009).
56. Molina-Mendoza, A. J. et al. Centimeter-scale synthesis of ultrathin layered MoO_3 by van der Waals Epitaxy. *Chem. Mater.* **28**, 4042–4051 (2016).
57. Carcia, P. F. & McCarron, E. M. Synthesis and properties of thin film polymorphs of molybdenum trioxide. *Thin Solid Films* **155**, 53–63 (1987).
58. McCarron, E. M. & Carcia, P. F. Properties of MoO_3 thin film polymorphs. *Mat. Res. Soc. Symp. Proc.* **77**, 319–326 (1987).
59. Kalantar-Zadeh, K. et al. Synthesis of nanometre-thick MoO_3 sheets. *Nanoscale* **2**, 429–433 (2010).
60. Reed, B. W., Williams, D. R., Moser, B. P. & Koski, K. J. Chemically tuning quantized acoustic phonons in 2D layered MoO_3 nanoribbons. *Nano Lett.* **19**, 4406–4412 (2019).
61. Liu, X. L., Zhang, X., Lin, M. L. & Tan, P. H. Different angle-resolved polarization configurations of Raman spectroscopy: A case on the basal and edge plane of two-dimensional materials. *Chinese Phys. B* **26**, 067802 (2017).
62. Py, M. A., Schmid, P. E. & Vallin, J. T. Raman scattering and structural properties of MoO_3. *Nuovo Cim. B Ser. 11* **38**, 271–279 (1977).
63. Kim, J. H. et al. van der Waals epitaxial growth of single crystal α-MoO_3 layers on layered materials growth templates. *2D Mater.* **6**, 015016 (2018).
64. Puebla, S., Mariscal-jim, A., Munuera, C. & Castellanos-gomez, A. Optical-based thickness measurement of MoO_3 nanosheets. *Nanomaterials* **10**, 1272 (2020).
65. Nikogosyan, D. N. Beta barium borate (BBO). *Appl. Phys. A* **52**, 359–368 (1991).
66. G. Elert. Refraction – The Physics Hypertextbook. https://physics.info/refraction/ (1998).
67. Papadopoulos, N. et al. Large birefringence and linear dichroism in TiS 3 nanosheets. *Nanoscale* **10**, 12424–12429 (2018).

68. Iguiñiz, N., Frisenda, R., Bratschitsch, R. & Castellanos-Gomez, A. Revisiting the buckling metrology method to determine the Young's modulus of 2D materials. *Adv. Mater.* **31**, 1–24 (2019).
69. Feicht, P. et al. Systematic evaluation of different types of graphene oxide in respect to variations in their in-plane modulus. *Carbon N.Y.* **114**, 700–705 (2017).
70. Kunz, D. A. et al. In-plane modulus of singular 2:1 clay lamellae applying a simple wrinkling technique. *ACS Appl. Mater. Interfaces* **5**, 5851–5855 (2013).
71. Kunz, D. A. et al. Space-resolved in-plane moduli of graphene oxide and chemically derived graphene applying a simple wrinkling procedure. *Adv. Mater.* **25**, 1337–1341 (2013).
72. Brennan, C. J., Nguyen, J., Yu, E. T. & Lu, N. Interface adhesion between 2D materials and elastomers measured by Buckle Delaminations. *Adv. Mater. Interfaces* **2**, 1–7 (2015).
73. Bowden, N., Brittain, S., Evans, A. G., Hutchinson, J. W. & Whitesides, G. M. Spontaneous formation of ordered structures in thin films of metals supported on an elastomeric polymer. *Nature* **393**, 146–149 (1998).
74. Terentjev, E. M. Precise determination of the Poisson ratio in soft materials with 2D digital image correlation. *Soft Matter* **9**, 6037–6045 (2013).
75. Šiškins, M. et al. Highly anisotropic mechanical and optical properties of 2D layered As2S3 membranes. *ACS Nano* **13**, 10845–10851 (2019).
76. Castellanos-Gomez, A. et al. Deterministic transfer of two-dimensional materials by all-dry viscoelastic stamping. *2D Mater.* **1**, 1–34 (2014).
77. Zhao, Q., Wang, T., Ryu, Y. K. & Frisenda, R. An inexpensive system for the deterministic transfer of 2D materials. *J. Phys. Mater.* **3**, 016001 (2020).
78. Frisenda, R. et al. Micro-reflectance and transmittance spectroscopy: a versatile and powerful tool to characterize 2D materials. *J. Phys. D. Appl. Phys.* **50**, aa5256 (2017).
79. Giannozzi, P. et al. {QUANTUM} {ESPRESSO}: a modular and open-source software project for quantum simulations of materials. *J. Phys. Condens. Matter* **21**, 395502 (2009).
80. Marini, A., Hogan, C., Gruening, M. & Varsano, D. yambo: An ab initio tool for excited state calculations. *Comput. Phys. Commun.* **180**, 1392–1403 (2009).
81. Sangalli, D. et al. Many-body perturbation theory calculations using the yambo code. *J. Phys. Condens. Matter* **31**, 325902 (2019).
82. Perdew, J. P., Burke, K. & Ernzerhof, M. Generalized gradient approximation made simple. *Phys. Rev. Lett.* **77**, 3865–3868 (1996).
83. Hamann, D. R. Optimized norm-conserving Vanderbilt pseudopotentials. *Phys. Rev. B* **88**, 85117 (2013).
84. Corso, A. D. https://dalcorso.github.io/thermo_pw/ (2020).

ACKNOWLEDGEMENTS

This project has received funding from the European Research Council (ERC) under the European Union's Horizon 2020 research and innovation programme (grant agreement n° 755655, ERC-StG 2017 project 2D-TOPSENSE), the European Commission, under the Graphene Flagship (Core 3, grant number 881603), the Spanish Ministry of Economy, Industry and Competitiveness through the grant MAT2017-87134-C2-2-R. R.F. acknowledges the support from the Spanish Ministry of Economy, Industry and Competitiveness (MINECO) through a Juan de la Cierva-formación fellowship 2017 FJCI-2017-32919. S.P. acknowledges the fellowship PRE2018-084818. R. D'A. acknowledges financial support from the grant Grupos Consolidados UPV/EHU del Gobierno Vasco (Grant No. IT1249-19), the support of the MICINN through the grant "SelectDFT" (Grant No. FIS2016-79464-P) and travel support from the MINECO grant "TowTherm" (Grant No. MINECOG17/A01). G.S.-S. acknowledges financial support from Spanish MICIU RTI2018-099054-J-I00 and MICINN IJC2018-038164-I. Electron microscopy observations were carried out at the Centro Nacional de Microscopia Electronica, CNME-UCM.

AUTHOR CONTRIBUTIONS

S.P. fabricated the MoO_3 flake samples and performed the optical microscopy, Raman spectroscopy and buckling metrology experiments. G.S-S., performed the electron microscopy experiments. R.F., C.M. and A.C.-G. supervised and designed the experiments. S.P., C.M. and A.C.-G. drafted the firsts version of the manuscript. R.D'A. developed the theoretical calculations. All authors contributed to writing the final version of the manuscript.

COMPETING INTERESTS

The authors declare no competing interests.

ADDITIONAL INFORMATION

Supplementary information The online version contains supplementary material available at https://doi.org/10.1038/s41699-021-00220-5.

Correspondence and requests for materials should be addressed to A.C-G.

Reprints and permission information is available at http://www.nature.com/reprints

Publisher's note Springer Nature remains neutral with regard to jurisdictional claims in published maps and institutional affiliations.